

Vol. 10 • No. 32 • November 14 • 2023

[www.advmatinterfaces.de](http://www.advmatinterfaces.de)

# ADVANCED MATERIALS INTERFACES

Open Access



# Impact of Silicon Ion Irradiation on Aluminum Nitride-Transduced Microelectromechanical Resonators

David D. Lynes,\* Joshua Young, Eric Lang, and Hengky Chandralalim\*

Microelectromechanical systems (MEMS) resonators use is widespread, from electronic filters and oscillators to physical sensors such as accelerometers and gyroscopes. These devices' ubiquity, small size, and low power consumption make them ideal for use in systems such as CubeSats, micro aerial vehicles, autonomous underwater vehicles, and micro-robots operating in radiation environments. Radiation's interaction with materials manifests as atomic displacement and ionization, resulting in mechanical and electronic property changes, photocurrents, and charge buildup. This study examines silicon (Si) ion irradiation's interaction with piezoelectrically transduced MEMS resonators. Furthermore, the effect of adding a dielectric silicon oxide (SiO<sub>2</sub>) thin film is unveiled. Aluminum nitride on silicon (AlN-on-Si) and AlN-SiO<sub>2</sub>-Si bulk acoustic wave (BAW) resonators are designed and fabricated. The devices are irradiated using 2 MeV Si<sup>+</sup> ions at various fluxes up to a total fluence of  $5 \times 10^{14} \text{ cm}^{-2}$ . A time anneal is conducted to characterize device recovery. Scattering (S-) parameters are measured in situ. Specific damage coefficients are derived to describe the radiation effect on resonant frequency ( $f_r$ ), quality factor (Q), motional resistance ( $R_m$ ), and electromechanical coupling factor ( $k_{\text{eff}}^2$ ). Furthermore, the damage coefficients for the bulk material properties of elastic modulus (E) and the piezoelectric coefficient ( $d_{31}$ ) are found.

## 1. Introduction

Microelectromechanical systems (MEMS) acoustic resonators have many uses, from radio frequency (RF) resonators, filters, and electronic oscillators<sup>[1–8]</sup> to inertial sensing<sup>[9–11]</sup> and environmental monitoring.<sup>[12,13]</sup> The large variety of device designs facilitates using MEMS resonators in applications such as energy harvesting,<sup>[14–16]</sup> signal processing,<sup>[17–19]</sup> health,<sup>[20,21]</sup> robotics,<sup>[22,23]</sup> defense,<sup>[22,24]</sup> and aerospace.<sup>[25]</sup> In general, MEMS sensors and filters have very low mass, power consumption, and smaller footprint than their bulk circuit component equivalents.<sup>[26,27]</sup> Aluminum nitride (AlN) is especially attractive as a transduction material for MEMS resonators. AlN can be integrated into the complementary metal-oxide-semiconductor (CMOS) fabrication process, maintaining the majority of its bulk physical, thermal, and electrical properties even as a thin film.<sup>[28]</sup> AlN largely retains its bulk physical, thermal, and electric properties as a thin film. Furthermore, AlN can be doped with other elements, such as

scandium, to increase electromechanical coupling or to add ferroelectric behavior.<sup>[29,30]</sup> AlN has been utilized in energy harvesters, actuators, RF filters, duplexers, and accelerometers as a piezoelectric transducer.<sup>[24,28,31,32]</sup> AlN has also been successfully implemented as part of the gate dielectric in thin film transistors (TFT).<sup>[33]</sup>

The ubiquity of these devices makes them ideal for use in systems that operate in space radiation environments, e.g., accelerometers used for inertial navigation and RF filters for communication in spacecraft systems are subject to radiation belts and cosmic rays.<sup>[34,35]</sup> Piezoelectric accelerometers and acoustic sensors in nuclear reactor instrumentation are subject to an elevated gamma and neutron environment.<sup>[36,37]</sup> Aerospace and power systems' sensors, signal processors, and energy harvesters require high sensitivity, high resolution, and low loss. As these devices are exposed to harsh vibration, thermal, and radiation environments, their properties can be altered or degraded. Establishing device resiliency and performance in a radiation environment is a critical tool for engineers in the system design process.

Heavy-charged particle radiation can be defined as irradiation with any particle heavier than a proton. In the natural space

D. D. Lynes, H. Chandralalim  
 Department of Electrical and Computer Engineering  
 Air Force Institute of Technology  
 Wright-Patterson Air Force Base, OH 45433, USA  
 E-mail: david.lynes.2@us.af.mil; hengky@microsystems.group

J. Young  
 Ion Beam Laboratory  
 Sandia National Laboratories  
 Albuquerque, NM 87123, USA

E. Lang  
 Department of Nuclear Engineering  
 The University of New Mexico  
 Albuquerque, NM 87131, USA

 The ORCID identification number(s) for the author(s) of this article can be found under <https://doi.org/10.1002/admi.202300240>

© 2023 The Authors. Advanced Materials Interfaces published by Wiley-VCH GmbH. This is an open access article under the terms of the Creative Commons Attribution License, which permits use, distribution and reproduction in any medium, provided the original work is properly cited.

DOI: 10.1002/admi.202300240

environment, high energy heavy ions manifest as cosmic rays or may originate from solar flares.<sup>[35]</sup> Alpha particles and other heavy secondary particles also result from nuclear reactions caused by astrophysical processes.<sup>[35]</sup> Analogous heavy-charged particle radiation might be generated in a laboratory environment. For radiation testing, heavy ion irradiation can be used to extrapolate the damage caused by protons or neutrons found in space or nuclear reactors to high damage levels (0.1–100 dpa) with a much lower particle fluence.

Heavy ion irradiation deposits its energy into materials via non-ionizing energy loss (NIEL) and ionization. NIEL is the transfer of momentum from the radiated particle to the atomic nuclei of the material, which can result in atoms being moved from their resting position in the lattice, leaving vacancies and creating interstitial defects.<sup>[34]</sup> These defects can modify the mechanical and electrical properties of the material. Displacement damage has been shown to alter the diffusion lengths and minority-carrier lifetimes in crystalline silicon.<sup>[35]</sup> Furthermore, the amorphization of crystalline silicon decreases its mass density and elastic modulus.<sup>[38–40]</sup> Ionization results in the generation of electron–hole pairs (EHP). Depending upon the material, this can increase material conductivity or trap charges causing localized electric fields. Previous work has shown that Aluminum Nitride on Silicon (AlN-on-Si) and Aluminum Nitride on Silicon Dioxide on Silicon (AlN-SiO<sub>2</sub>-Si)-based BAW resonators are strongly resistant to the effects of EHP generation compared to electrostatic or capacitive MEMS, where charge accumulation effects dominate.<sup>[41–43]</sup> This work focuses on the displacement damage effects caused by heavy particle radiation.

Over the past 60 years, considerable research has gone into the effects of radiation on (metal-oxide-semiconductor) MOS devices; well-established theory and experimental data exist that describe MOS device behavior in a radiation environment.<sup>[35]</sup> However, due to the immaturity of the MEMS field and the vast range of materials, technologies, and applications, no universally accepted test procedure or characterization standard exists for the effects of radiation on MEMS.<sup>[27]</sup> Early radiation effects research efforts on MEMS focused on commercial-off-the-shelf (COTS) accelerometers.<sup>[41]</sup> Some recent work has measured the performance of piezoelectric sensors in neutron and gamma environments, the effects of space radiation on MEMS insulators, gamma radiation effects on piezoresistive pressure sensors, accelerometer performance in nuclear reactors, and changes in the mechanical characteristics.<sup>[24,37,44–46]</sup> The influence of X-ray radiation on the gauge factors of statically suspended GaN/AlN beams has also been reported.<sup>[47]</sup>

Nearly all existing research<sup>[48–51]</sup> characterizes MEMS behavior pre- and post-irradiation but does not capture how device performance changes throughout the irradiation period. This work presents a method of determining damage coefficients that may be used to predict changes to MEMS resonator performance characteristics due to radiation in a similar fashion to what has been completed for Si bipolar and MOS technology (i.e., threshold voltage shifts, open circuit current, carrier lifetime).<sup>[35,52]</sup> In the study presented here, virgin, in situ, and post-irradiation measurements were performed to better understand piezoelectrically transduced MEMS resonator response to heavy ion irradiation.

In this study, silicon ions were selected due to their chemical inertness with the materials utilized in the device, thus mitigat-

ing the risk of nuclear activation. Ionization, a consequence of bombardment from any heavy ion, is notably maximized with silicon irradiation in comparison to lighter ions such as carbon. For the purposes of observing changes in both the effective Young's modulus and the piezoelectric coefficient, a majority of vacancies should be created in the piezoelectric layer, disrupting the crystalline structure of AlN. Additionally, for further examination of the effects of the added silicon dioxide layer, it is beneficial to have a smaller portion of the silicon ions penetrate more deeply into the resonator body.

To identify the optimal energy for irradiation, Transport of Ions in Matter (TRIM) simulations were conducted, which pinpointed 2 MeV as the optimal energy. With this energy, approximately half of the vacancies would be expected to occur in the AlN layer, while ≈10% would occur in the silicon or oxide layer.

Electrical measurements of the scattering (S-) parameters were collected for the virgin system, in situ during irradiation, post-irradiation, and timed anneal. Material analysis was performed pre- and post-irradiation by Raman spectroscopy, electron backscatter diffraction (EBSD), and transmission electron microscopy (TEM). Specific damage coefficients are derived to describe the radiation effect on resonant frequency ( $f_r$ ), quality factor ( $Q$ ), motional resistance ( $R_m$ ), and electromechanical coupling factor ( $k_{\text{eff}}^2$ ). Furthermore, the derivation of damage coefficients for the bulk material properties of elastic modulus ( $E$ ) and the piezoelectric coefficient ( $d_{31}$ ) is shown.

As depicted in **Figure 1**, AlN-on-Si and AlN-SiO<sub>2</sub>-Si bulk acoustic wave resonators were irradiated with 2 MeV Si<sup>+</sup> ions up to a fluence of  $5 \times 10^{14} \text{ cm}^{-2}$  at different ion fluxes at the Sandia National Laboratories' (SNL) Ion Beam Laboratory (IBL).

## 2. Bulk Acoustic Wave Resonators

Bulk Acoustic Wave (BAW) resonators exploit acoustic waves that propagate throughout the entire solid body, hence the term “bulk”. The Width Extensional Mode (WEM) is a subset of BAW. As shown in **Figure 2a**, the WEM of a rectangular flat plate resonator is a longitudinal wave that travels the width of the bar, causing it to expand and contract. The WEM can be described by the 1D wave equation with Neumann boundary conditions such that its fundamental resonant frequency is given by:

$$f_r = \frac{1}{2W} \sqrt{\frac{E_{\text{eff}}}{\rho_{\text{eff}}}} \quad (1)$$

where  $W$  is the width,  $E_{\text{eff}}$  is the effective Young's modulus (also called the elastic modulus), and  $\rho_{\text{eff}}$  is the effective density of the stack forming the bar.<sup>[53]</sup> For the case of the two-port piezoelectric-on-Si resonator, the bulk component RLC circuit equivalents of motional resistance ( $R_m$ ), capacitance ( $C_m$ ), and inductance ( $L_m$ ) are given by:

$$R_m = \frac{\pi}{4} \frac{T}{L} \frac{\sqrt{E_{\text{eff}} \rho_{\text{eff}}}}{QE_{\text{piezo}}^2 d_{31}^2} \quad C_m = \frac{4}{\pi^2} \frac{LW}{T} \frac{E_{\text{piezo}}^2}{E_{\text{eff}}} d_{31}^2$$

$$L_m = \frac{\rho_{\text{eff}}}{E_{\text{piezo}}^2} \frac{TW}{L} \frac{1}{4d_{31}^2} \quad (2)$$

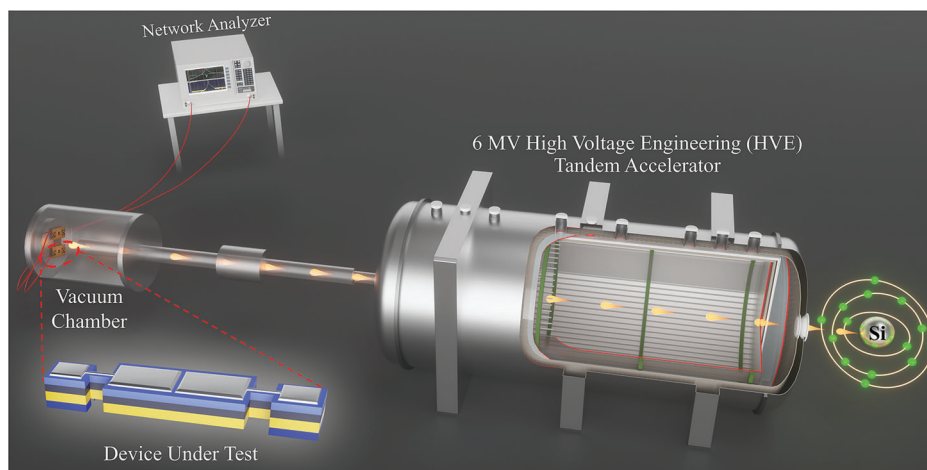
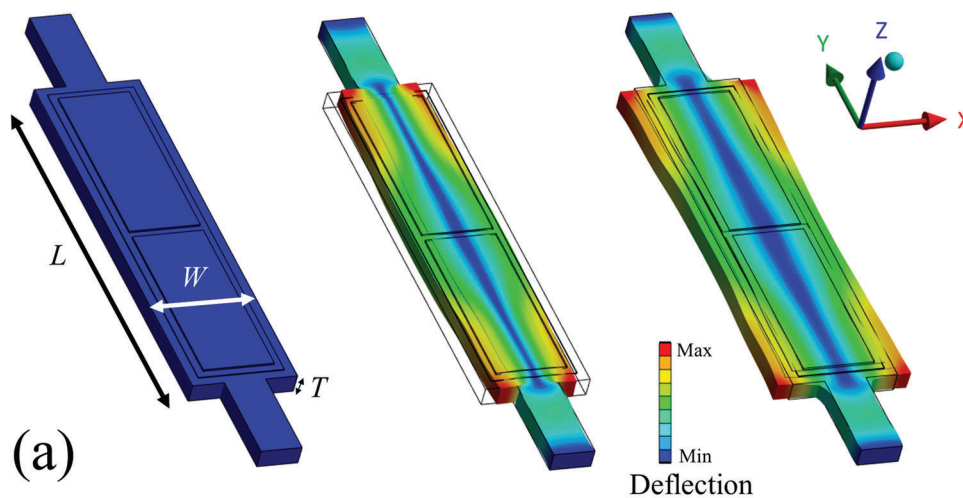
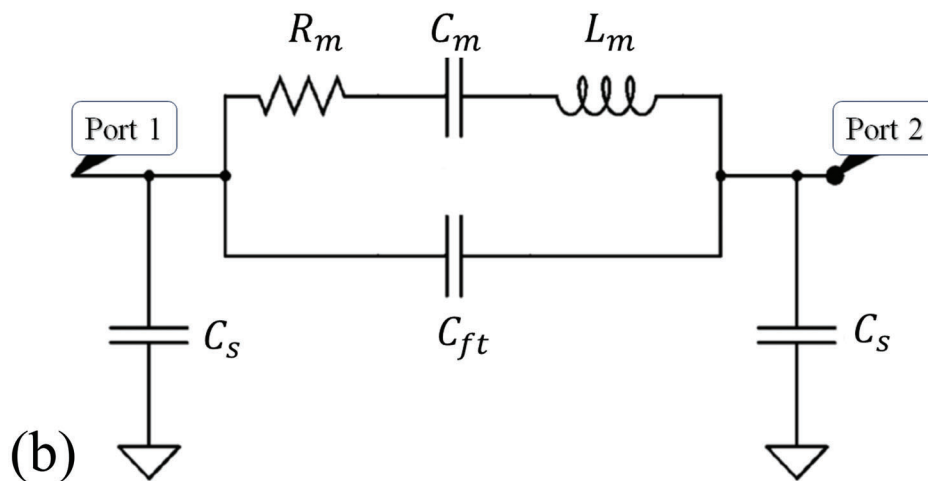


**Figure 1.** Illustration of the experimental setup. The High Voltage Engineering (HVE) Tandem Accelerator system generates and steers the 2 MeV Si<sup>+</sup> ions toward the target. The resonators, mounted on the custom printed circuit board (PCB) are placed inside the vacuum chamber. Feedthroughs with RF connections inside the chamber allow for in situ measurement of S-parameters via a network analyzer outside the chamber.



(a)



(b)

**Figure 2.** a) Illustration of a rectangular flat plate resonator and the motion of the 1st or fundamental width extensional mode (WEM) vibration. Key dimensions of length ( $L$ ), width ( $W$ ), and thickness ( $T$ ) are shown. b) A schematic of the Modified Butterworth Van Dyke (MBVD) electrical equivalent circuit model that represents the AlN-transduced WEM resonator.

where  $E_{\text{piezo}}$  is the Young's modulus of the piezoelectric film,  $Q$  is the quality factor, and  $d_{31}$  is the piezoelectric coefficient that actuates the WEM vibration.<sup>[54]</sup> Finally, from the series electrical resonant circuit, we have the relationships:

$$(QR_m)^2 = \frac{L_m}{C_m} \frac{1}{(2\pi f_r)^2} = L_m C_m \quad (3)$$

The Modified Butterworth Van Dyke (MBVD) electrical equivalent circuit model that is commonly used to represent the behavior of a piezoelectric resonator is shown in Figure 2b.

It has been shown that the elastic modulus of amorphous Si is roughly 50% of that of crystalline Si.<sup>[38,39]</sup> Other work has shown that the difference in mass density between amorphous and crystalline Si is only  $\approx 2\%$ . Furthermore, the maximum ion fluence of this experiment only increases the bulk atomic density by  $\approx 10$  ppm (0.001%). Therefore, the change in material mass density and resonator dimensions are assumed to be negligible compared to the change to the bulk material properties of elastic moduli and piezoelectric constants. This conclusion aligns consistently with prior studies examining the effects of ion radiation on MEMS resonators.<sup>[49,51]</sup> Thus, by Equations (1)–(3), the relationship between the product  $E_{\text{piezo}}d_{31}$ , and  $L_m$ , and  $C_m$  can be expressed as:

$$\frac{E_{\text{piezo}}d_{31}}{E_{\text{piezo}_0}d_{31_0}} = \sqrt{\frac{f_r R_{m_0} Q_0}{f_{r_0} R_m Q}} = \sqrt{\frac{L_{m_0}}{L_m}} = \frac{f_r}{f_{r_0}} \sqrt{\frac{C_m}{C_{m_0}}} \quad (4)$$

where the subscript  $_0$  indicates the pre-irradiation value. This paper uses the subscript  $_0$  to indicate the pre-irradiation value.

A first-order differential equation approximates the defect concentration within a material undergoing irradiation. The time rate of change in defect concentration ( $D$ ) is given as the number of defects caused per incident radiation particle in a pure material ( $\kappa$ ) minus the defect ratio ( $D(t)/D_{\text{sat}}$ ). This value is multiplied by the flux of the radiation particles ( $\phi$ ).  $D_{\text{sat}}$  represents the number of defects when the material is saturated. In other words,  $D_{\text{sat}}$  is the maximum number of defects possible for a given radiation and target material. Thus, as defect concentration increases, the incident particle or its knock-on atoms are more likely to hit an already displaced atom and not cause a new defect:

$$\frac{dD(t)}{dt} = \kappa \left( 1 - \frac{D(t)}{D_{\text{sat}}} \right) \phi \quad (5)$$

which, assuming some initial defect concentration  $D_0$ , has the solution:

$$D(t) = (D_0 - D_{\text{sat}}) e^{-\frac{\kappa\phi}{D_{\text{sat}}}t} + D_{\text{sat}} \quad (6)$$

Both  $D_0$  and  $D_{\text{sat}}$  are challenging to measure directly. Therefore, this relationship is better viewed as the ratio between the two:

$$\frac{D(\Phi)}{D_0} = (1 - \alpha) e^{-\frac{\Phi}{\tau}} + \alpha \quad (7)$$

where  $\alpha = D_{\text{sat}}/D_0$ ,  $\tau = D_{\text{sat}}/\kappa$  represents the decay constant and  $\Phi = \phi t$  is the fluence of the radiation particles. Because previous work has demonstrated that dislocation damage is the dominant effect of radiation on piezo-on-Si devices, it is reasonable to extrapolate Equation (7) to describe the change in any bulk mechanical property as a function of radiation dose or fluence by replacing  $D$  with the property such as  $E_{\text{eff}}$  or  $d_{31}$ .<sup>[43]</sup> Then,  $\alpha$  and  $\tau$  become damage coefficients specific to that property and type of radiation in the target material.

### 3. Experimental Section

Two-port AlN transduced rectangular flat plate MEMS resonators were used in this experiment because of their straightforward analytical descriptions of behavior. Two designs were used, one that consisted of AlN on top of Si and another with a SiO<sub>2</sub> thin film sandwiched between the AlN and Si layers. From bottom to top, the resonators consisted of a 10  $\mu\text{m}$  thick phosphorous doped Si (n-Si) layer, the optional 0.2  $\mu\text{m}$  SiO<sub>2</sub> film, a 0.5  $\mu\text{m}$  AlN layer, and 0.02  $\mu\text{m}$  chromium (Cr) and 1.0  $\mu\text{m}$  Al to act as the top conductor. The layers and materials are illustrated in Figure 3. The devices were fabricated using the PiezoMUMPs process by MEMSCAP Inc. Nominal device dimensions are presented in Table 1. Cross-sectional scanning electron micrographs of the two resonators are shown in Figure 3c,f. The devices were mounted to a custom printed circuit board (PCB) to prepare them for irradiation and allow for simultaneous measurement of S-parameters. The devices were laser diced and secured to the PCB using conductive silver paste. 99% Au 1-mil bonding wires were used for wirebonding. 50  $\Omega$  SubMiniature version A (SMA) connectors were soldered to the PCB to provide an RF cable connection. Images of the prepared devices are provided in the Supporting Information.

Heavy ion irradiation was accomplished using 2 MeV Si<sup>+</sup> ions. Si was chemically inert with the device materials and does not result in activation (i.e., making them radioactive). Heavy ion irradiation results in ionization that decreases with depth, and vacancy production, which increases with depth, with a maximum at the Bragg peak or ion end of range (EOR). Frenkel Pairs and defect clusters were produced, particularly at the EOR. This atomic displacement damage creates electrical traps in electronic materials and modifies the material properties.

Transport of Ions in Matter (TRIM) simulations were performed to estimate the vacancy production in the device. TRIM uses specific values of displacement energy for each element to determine if sufficient energy was transferred to the atom to displace it by more than one lattice site. Displacement energies used for constituent elements were tabulated in the Supporting Information. The simulation was optimized to produce maximum vacancy in the AlN layer while causing significant displacements in the lower SiO<sub>2</sub> or Si layers. The Ion Distribution and Quick Calculation of Damage parameters were used to estimate the damage based on the Kinchin–Pease method.<sup>[55]</sup> For 2 MeV Si<sup>+</sup> ions, simulation results showed  $\approx 50\%$  of dislocations in the AlN layer and 10% in the lower Si or SiO<sub>2</sub>

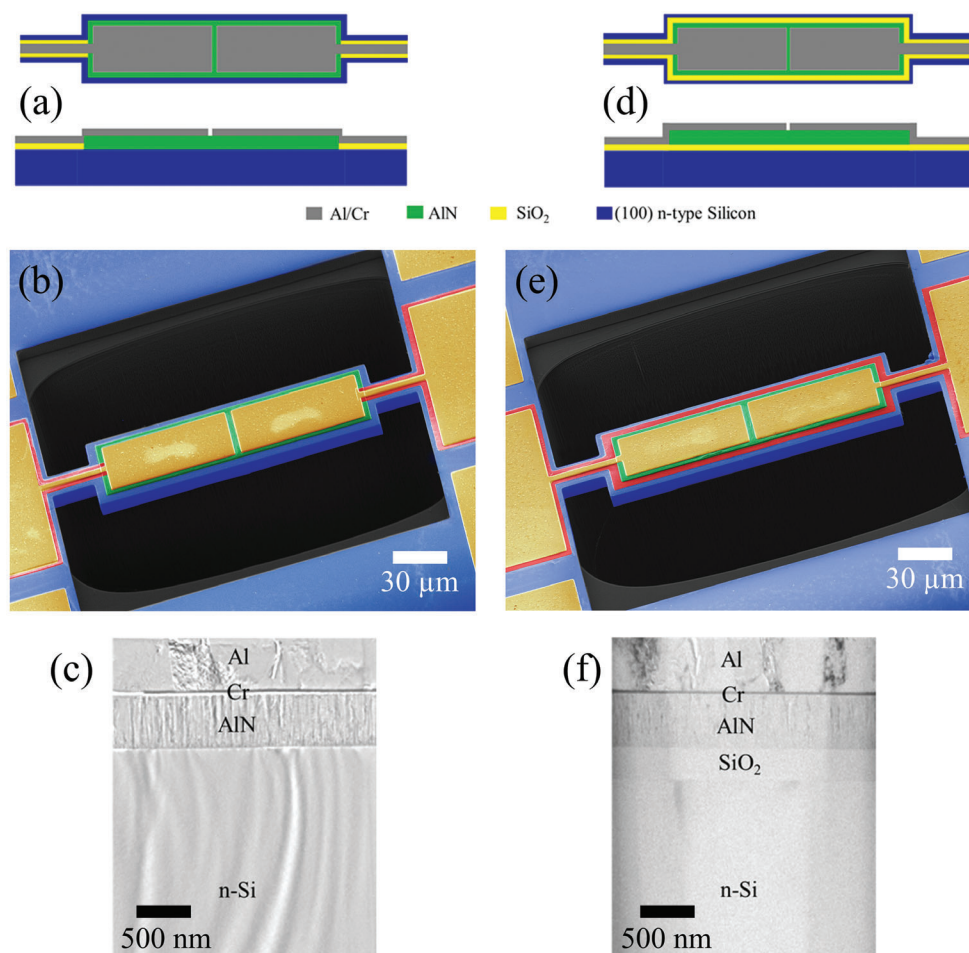


**Figure 3.** The two AIN transduced rectangular flat plate resonator designs. (a) The AIN-on-Si design. (d) The AIN-SiO<sub>2</sub>-Si design. Layer thicknesses were: 1.02 μm – Al/Cr, 0.5 μm – AIN, 0.2 μm – SiO<sub>2</sub> (optional), and 10 μm – n-Si. (b) and (e) Colorized scanning electron microscope (SEM) images of AIN-on-Si and AIN-SiO<sub>2</sub>-Si resonators. (c) and (f) Cross-sectional SEM images of AIN-on-Si and AIN-SiO<sub>2</sub>-Si resonators.

layer. The results from the TRIM simulations are presented in **Figure 4**.

The devices were irradiated at the SNL IBL using the HVE 6 MV tandem accelerator. The devices were irradiated one at a time. Irradiation was performed at room temperature at an average pressure of 1 μTorr. Connections in the vacuum chamber allowed for RF cables to be connected so that S-parameters could be recorded in situ. S-parameters were recorded by a network analyzer outside the chamber, as shown in **Figure 1**. Short-open-load-through (SOLT) calibration of the network analyzer was performed before placing the samples in the chamber to remove cable and connector losses. Virgin characteristics for both devices were taken followed by irradiation up to a fluence of  $5 \times 10^{14} \text{ cm}^{-2}$  at a flux of

$1.9 \times 10^{11} \text{ cm}^{-2} \text{ s}^{-1}$ . A 30 min time anneal in vacuum was recorded for one of each device design after irradiation. To observe the effects of different fluxes, additional devices of the same design were irradiated with identical parameters at a higher flux of  $4.7 \times 10^{11} \text{ cm}^{-2} \text{ s}^{-1}$ .

Following data collection, resonator properties were extracted from the S-parameters. Resonant frequency,  $f_r$ , and anti-resonant frequency,  $f_a$ , are measured directly from the input admittance, Y<sub>11</sub>. The single electrode one port electromechanical coupling coefficient ( $k_{\text{eff}}^2$ ) is defined as:

$$k_{\text{eff}}^2 = \frac{f_a^2 - f_r^2}{f_a^2} \quad (8)$$

**Table 1.** Layer dimensions for AIN-on-Si and AIN-SiO<sub>2</sub>-Si rectangular flat plate resonators.

Parameter	Al/Cr	AIN	SiO <sub>2</sub>	n-Si
No SiO <sub>2</sub> Layer Dimensions L × W × T in μm	97 × 37 × 1.02	206 × 46 × 0.5	Not Applicable	216 × 56 × 10
With SiO <sub>2</sub> Layer Dimensions L × W × T in μm	97 × 37 × 1.02	206 × 46 × 0.5	216 × 56 × 0.2	222 × 62 × 10

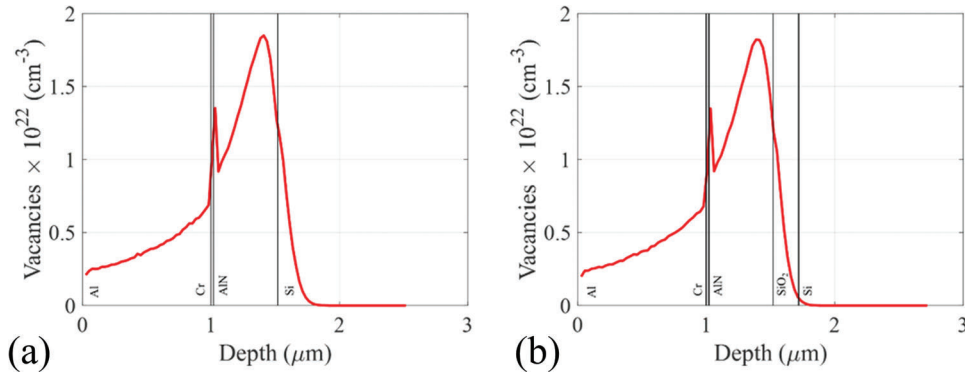


**Figure 4.** Results of TRIM simulations of 2 MeV Si<sup>+</sup> ions into the devices. Vacancy density versus ion depth is shown for a) the AlN-on-Si resonator and b) the AlN-SiO<sub>2</sub>-Si resonator.

The motional resistance,  $R_m$ , of the two-port resonator is measured using:

$$R_m = 2Z_0 \left( 10^{\frac{IL}{20}} - 1 \right) \quad (9)$$

where  $IL$  is the insertion loss in dB at resonance of the forward transmission parameter,  $S_{21}$  and  $Z_0$  is the termination impedance of the measurement setup.<sup>[53,56]</sup> Finally, the unloaded quality factor,  $Q$ , is extracted using:

$$Q = \frac{Q_L}{\left( 1 - 10^{-\frac{IL}{20}} \right)} \quad (10)$$

where  $Q_L = f_r/BW_{-3}$  is the loaded quality factor where  $BW_{-3}$  is the  $-3$  dB bandwidth of the resonance peak.<sup>[56]</sup>

## 4. Results

The frequency response of the six resonators at the fundamental WEM mode was recorded during ion irradiation. **Figure 5** presents graphs of the  $S_{21}$  transmission response for both resonators as a function of fluence, plotted from an initial zero fluence state. The dashed lines in the figure are projections of  $f_r$

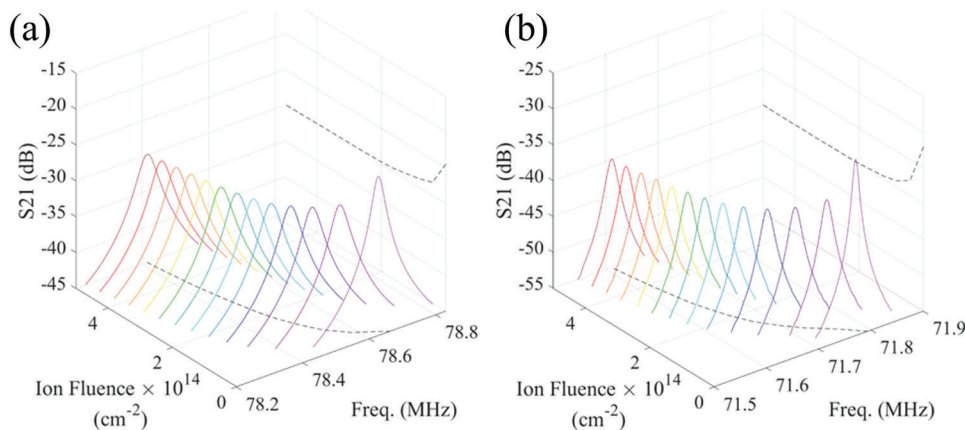


**Figure 5.** Measured  $S_{21}$  frequency response for the rectangular flat plate resonators as a function of fluence for a) AlN-on-Si and b) AlN-SiO<sub>2</sub>-Si designs.  $f_r$  and  $IL$  are projected and shown as the dashed lines.  $f_r$  and  $IL$  both behave as decaying exponentials.

and  $IL$ . From this example, the decaying exponential behavior of the resonator characteristics starts to become apparent. The measured values of  $f_r$ ,  $R_m$ ,  $Q$ , and one port  $k_{\text{eff}}^2$  for the resonators after irradiation to a fluence of  $5 \times 10^{14} \text{ cm}^{-2}$  at a flux of  $1.9 \times 10^{11} \text{ cm}^{-2} \text{ s}^{-1}$  are presented in the Supporting Information. The expected decaying exponential characteristic of  $R_m$ ,  $Q$ , and  $k_{\text{eff}}^2$  can be seen clearly in these data; however, to compare the different device designs it is more beneficial to examine the fractional shift of the parameters (**Figure 6**).

The fractional shift data are of the form  $X(\Phi)/X_0$  where  $X(\Phi)$  is the measured value at fluence  $\Phi$  and  $X_0$  is the pre-irradiation value. The data are presented in Figure 6. The data are fit to Equation (7), and their corresponding damage coefficients are presented. The decay constant,  $\tau$ , was reasonably consistent across parameters. That is, there was little difference in decay time between device designs, but the magnitude of the change differed significantly. During the course of irradiation, we observed a reduction in the fundamental resonant frequency, amounting to  $\approx 0.3\%$ , across both variants of the resonator. The resonator lacking an oxide layer exhibited a doubling of motional resistance, a decline in quality factor by  $>42\%$ , and an increase in single-port  $k_{\text{eff}}^2$  by  $>1.6$  times. Conversely, the device equipped with an oxide film demonstrated a  $>2.6$ -fold increment in  $R_m$ , while  $Q$  was reduced by more than

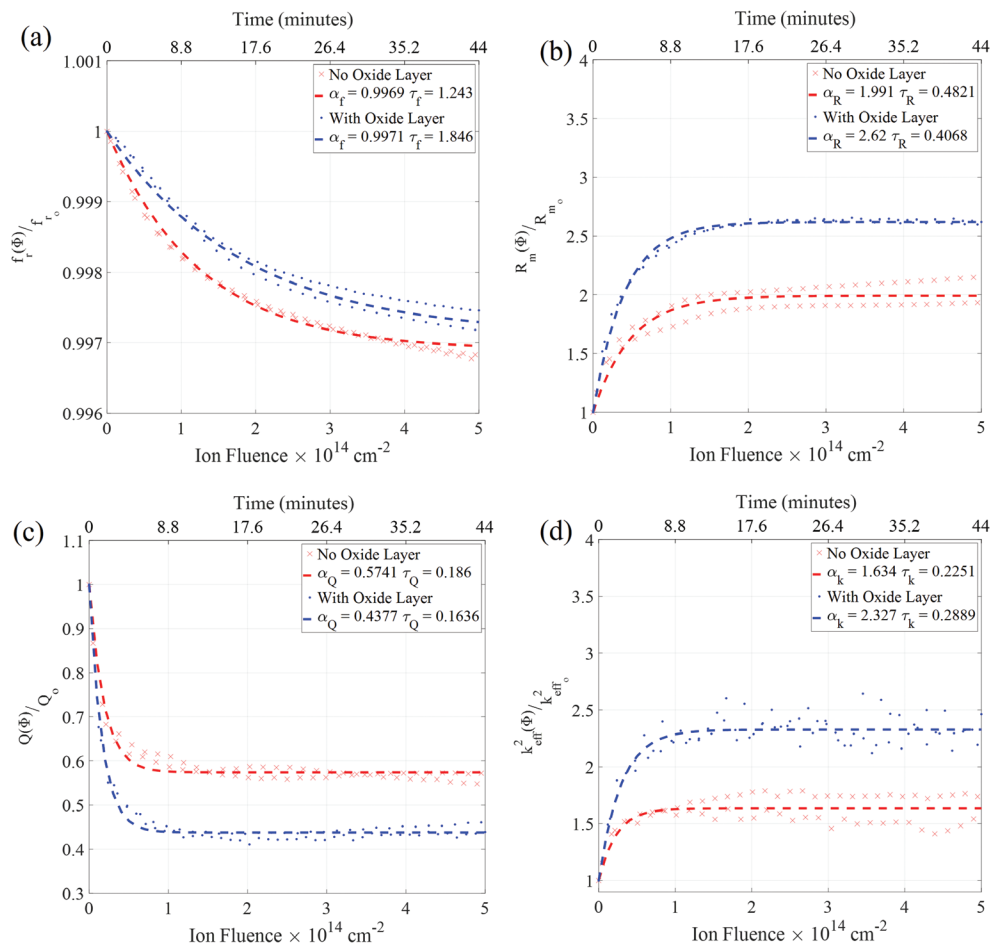


**Figure 6.** Measured fractional shifts for a)  $f_r$ , b)  $R_m$ , c)  $Q$ , d) and one port  $k_{\text{eff}}^2$  for AlN-based rectangular flat plate resonators irradiated by 2 MeV Si<sup>+</sup> ions at a flux of  $1.9 \times 10^{11} \text{ cm}^{-2} \text{ s}^{-1}$ . Also presented are the data fit to Equation (7) and the corresponding damage coefficients for each parameter. For clarity, only one out of every ten datapoints is plotted.

half. Nonetheless, the  $k_{\text{eff}}^2$  for this device still increased by over two-fold.

Two additional resonators (one of each design) were irradiated at a higher flux. The resonators were irradiated up to  $5 \times 10^{14} \text{ cm}^{-2}$  at a rate of  $4.7 \times 10^{11} \text{ cm}^{-2} \text{ s}^{-1}$ . The data are presented in Figure 7. There is little difference in the behavior of  $f_r$  at the higher flux. However, the magnitude of the fractional shift is less for all other measured parameters at the higher flux, as can be seen in Table 2 for  $R_m$ ,  $Q$ , and  $k_{\text{eff}}^2$ . The  $\alpha$  values indicate that the full fractional shift is less than that from the low flux experiments. Furthermore, the decay constant,  $\tau$ , is larger for the higher flux for the  $R_m$ ,  $Q$ , and  $k_{\text{eff}}^2$  parameters. Finally, the device with the oxide layer continued to be well described by Equation (7). The device without the oxide layer has a rapid exponential decay up to a fluence of  $0.5 \times 10^{14} \text{ cm}^{-2}$  followed by a linear decay that is attributable to the higher flux increasing the thermal energy within the device. The annealing rate increases as thermal energy is increased, as well described by the Arrhenius equation.<sup>[57]</sup> The results observed in this experiment are similar to those conducted for

polymers under irradiation at different fluxes. The magnitude of the change to many mechanical properties due to radiation to a specified dose or fluence was less at higher rates than at lower rates.<sup>[58,59]</sup>

Following irradiation, by 2 MeV Si<sup>+</sup> ions at  $1.9 \times 10^{11} \text{ cm}^{-2} \text{ s}^{-1}$  up to the  $5 \times 10^{14} \text{ cm}^{-2}$  total fluence, two devices (one of each design) were kept in the chamber under vacuum at room temperature to measure recovery. The results are presented in Figure 8. Presented are the change in parts per million (ppm) or percent of the parameter value at the end of irradiation. In this case, recovery is also well described by the decaying exponential model:  $\alpha(1 - e^{-\frac{t}{\tau}})$ .

The changes in the performance of resonators (with and without oxide layer), following exposure to various fluxes of silicon ion irradiation and subsequent room-temperature recovery, were quantitatively assessed. This evaluation involved measuring the fractional shifts in the resonant frequency, motional impedance, quality factor, and electromechanical coupling coefficient of the resonators. The results of these measurements are summarized in Table 3.

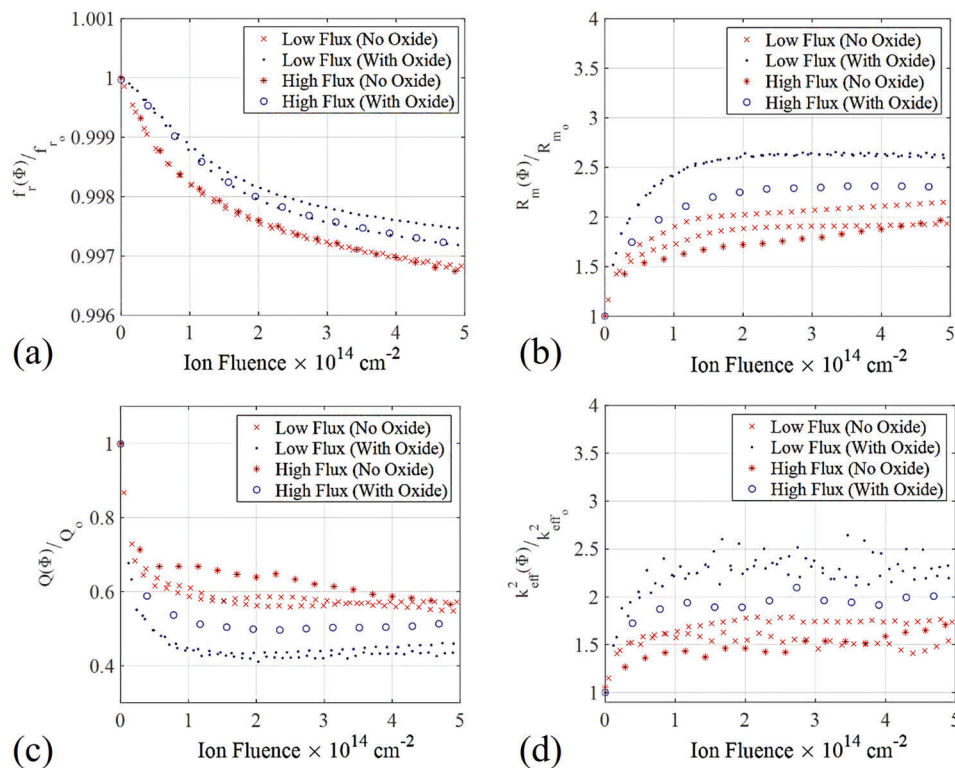


**Figure 7.** The measured fractional shifts of resonators exposed to a low flux ( $1.9 \times 10^{11} \text{ cm}^{-2} \text{ s}^{-1}$ ) and high flux ( $4.70 \times 10^{11} \text{ cm}^{-2} \text{ s}^{-1}$ ). Shown clockwise are a)  $f_r$ , b)  $R_m$ , c)  $Q$ , d) and  $k_{\text{eff}}^2$ . For clarity, only one out of every 10 datapoints are plotted.

## 5. Discussion

The thermal effects of the irradiation are decoupled from the results. It has been shown that the thermal effects on these devices are reversible and have minimal hysteresis.<sup>[60]</sup> AlN is highly resistant to thermal spike damage, and the thermal spikes are insufficient to melt Si.<sup>[61]</sup> The slight post-irradiation recovery shows that the thermal effects are minimal compared to the effects of atomic displacement damage.

To explore the physical changes, the fractional changes to the anti-resonance frequency ( $f_a$ ),  $L_m$ ,  $C_m$ , and the product  $E_{\text{piezo}}d_{31}$  during irradiation are extracted. The results are presented in **Figure 9**. For both device designs, the shift of  $f_a$  is slightly slower and of less magnitude to  $f_r$ . It can be seen by examining the product  $E_{\text{piezo}}d_{31}$  in **Figure 9b** that the magnitudes of the fractional shift and decay time are remarkably similar, albeit the device without the oxide layer experiences a more significant variance in results. This similarity supports the TRIM simulation data presented in **Figure 3**. The effects caused by the  $\text{Si}^+$  ions in the AlN

layer may be considered uniform between the two device designs. The increase in motional inductance,  $L_m$  is equivalent to an increase in the effective mass of an equivalent spring-mass-damper system.<sup>[8]</sup> The decrease to motional capacitance,  $C_m$  is akin to an increase in the effective spring constant of the equivalent spring-mass-damper system.<sup>[8]</sup>

The amorphous silicon dioxide layer experiences less disruption due to irradiation-induced atomic displacement since it is intrinsically amorphous. This characteristic bestows upon it a certain stability, leading to more consistent radiation responses in resonators that include this oxide film. In contrast, resonators without the amorphous oxide layer, which originally comprise crystalline silicon, undergo more pronounced atomic displacement or amorphization. This condition makes such devices more susceptible to variance in their radiation response.

The one port static capacitance,  $C_s$ , may be extracted using the following:  $C_s \approx C_m/k_{\text{eff}}^2$  such that the fractional change is:  $C_s/C_{s0} = (C_m/C_{m0}) (k_{\text{eff}0}^2/k_{\text{eff}}^2)$ .<sup>[53,62]</sup> The fractional change to  $C_s$  is presented in **Figure 10**. The fractional shift to  $C_s$  is quite

**Table 2.** Damage coefficients in accordance with the first order differential approximation for high and low flux experimental data.

Parameter	$f_r$		$R_m$ (2 port)		$Q$ (2 port)		$k_{\text{eff}}^2$ (1 port)	
	Low Flux	High Flux	Low Flux	High Flux	Low Flux	High Flux	Low Flux	High Flux
No $\text{SiO}_2$ Layer	$\alpha = 0.9969$ $\tau = 1.243$	$\alpha = 0.9968$ $\tau = 1.354$	$\alpha = 1.991$ $\tau = 0.4821$	$\alpha = 1.851$ $\tau = 0.759$	$\alpha = 0.5741$ $\tau = 0.186$	$\alpha = 0.618$ $\tau = 0.2234$	$\alpha = 1.634$ $\tau = 0.2251$	$\alpha = 1.506$ $\tau = 0.2752$
With $\text{SiO}_2$ Layer	$\alpha = 0.9971$ $\tau = 1.846$	$\alpha = 0.997$ $\tau = 1.866$	$\alpha = 2.620$ $\tau = 0.4068$	$\alpha = 2.294$ $\tau = 0.5188$	$\alpha = 0.4377$ $\tau = 0.1636$	$\alpha = 0.5066$ $\tau = 0.202$	$\alpha = 2.327$ $\tau = 0.2889$	$\alpha = 1.959$ $\tau = 0.3306$

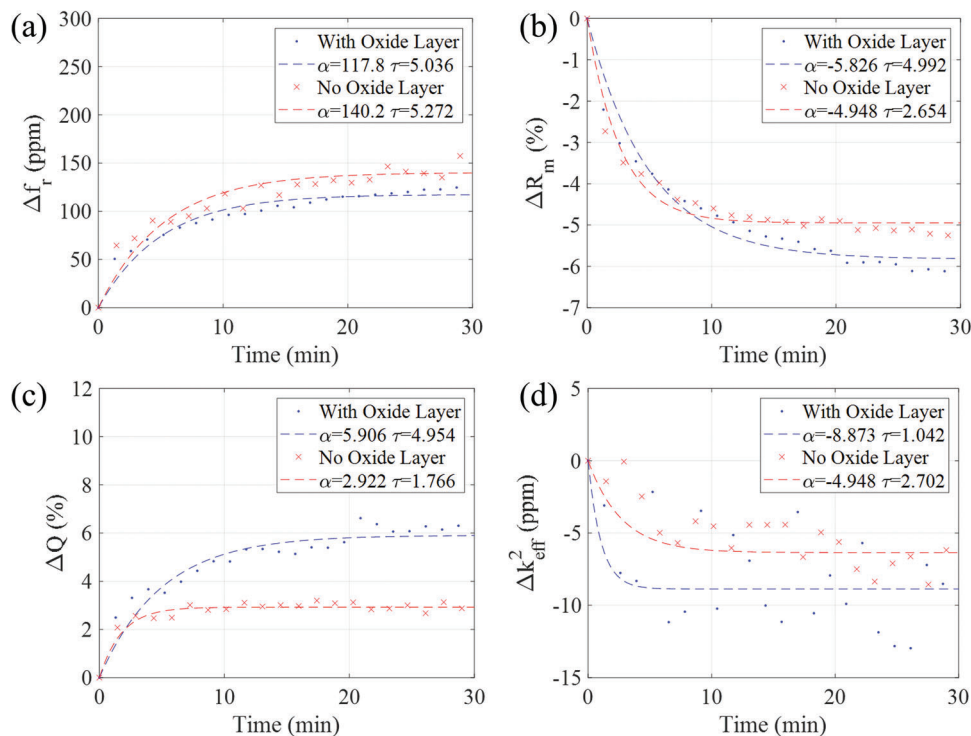


**Figure 8.** The measured fractional shifts of the recovery of resonator parameters after being exposed to  $5 \times 10^{14} \text{ cm}^{-2}$  at  $1.9 \times 10^{11} \text{ cm}^{-2} \text{ s}^{-1}$ . Clockwise are a)  $f_r$ , b)  $R_m$ , c)  $Q$ , d) and  $k_{\text{eff}}^2$ . For clarity, only one out of every five datapoints are plotted.

significant compared to the other parameters, most closely resembling the fractional shift to  $Q$ . Unlike  $f_r$ ,  $E_{\text{piezo}}d_{31}$ ,  $L_m$ , or  $C_m$ , the shift is abrupt and then remains stable. Assuming the change to the device surface area and distance between electrodes is negligible, the most prominent effect is then on the permittivity of the material between the electrodes. Creating Frenkel pairs and defect clusters in the AlN and amorphous  $\text{SiO}_2$  layers decreases the permittivity constant of the dielectric layers greater than the case where no oxide layer is present. Finally, feedthrough capacitance,  $C_{\text{ft}}$ , represents the system's capacitance when the input frequency is far from the resonant frequency, thereby making the impedance of the series  $R_m L_m C_m$  circuit infinite. During irradiation, there was a detectable change in feedthrough capacitance for the device without the oxide layer. However, the device with the oxide layer did not have a measurable change in feedthrough capacitance.

The structural composition of both resonator types considered in this study is dominated by a silicon device layer of  $10 \mu\text{m}$  thick-

ness. In accordance with the TRIM simulations and material characterizations delineated in the Supporting Information, we anticipate approximately half of the vacancies to manifest in the AlN layer, while  $\approx 10\%$  are expected in the silicon or oxide layer. These projections result in only minor fluctuations in the acoustic velocities of both types of resonators pre- and post-irradiation. As a result, we have recorded only marginal shifts in the resonant frequency for both types of devices—those with and without oxide layers—as graphically reported in Figures 6 and 7 and summarized in Table 3.

Material characterizations, including Raman spectroscopy, Electron Backscatter Diffraction, and Transmission Electron Microscopy, were performed pre- and post-irradiation. These analyses are detailed in the Supporting Information section. These conducted examinations provide quantifiable indications of the emergence of new atomic defects, triggered by  $\text{Si}^+$  ion irradiation. These defects contributed to the deterioration of the resonators' quality factors as a function of

**Table 3.** Tabulated performance variations in resonators exposed to silicon ion irradiation at high and low fluxes, and post room-temperature recovery.

	Low Flux [ $1.9 \times 10^{11} \text{ cm}^{-2} \text{ s}^{-1}$ ]		High Flux [ $4.7 \times 10^{11} \text{ cm}^{-2} \text{ s}^{-1}$ ]		30 min Room Temp Recovery	
	With Oxide	Without Oxide	With Oxide	Without Oxide	With Oxide	Without Oxide
$\frac{\Delta f}{f_0}$	-0.27%	-0.31%	-0.28%	-0.32%	0.324 ppm	0.434 ppm
$\frac{\Delta R_m}{R_{m0}}$	261.90%	199.10%	233.10%	199.10%	-15.74%	-9.95%
$\frac{\Delta Q}{Q_0}$	-56.23%	-42.59%	-47.40%	-42.60%	2.84%	1.38%
$\frac{\Delta k_{\text{eff}}^2}{k_{\text{eff}0}^2}$	232.70%	163.40%	199.90%	173.70%	-0.18%	-0.10%

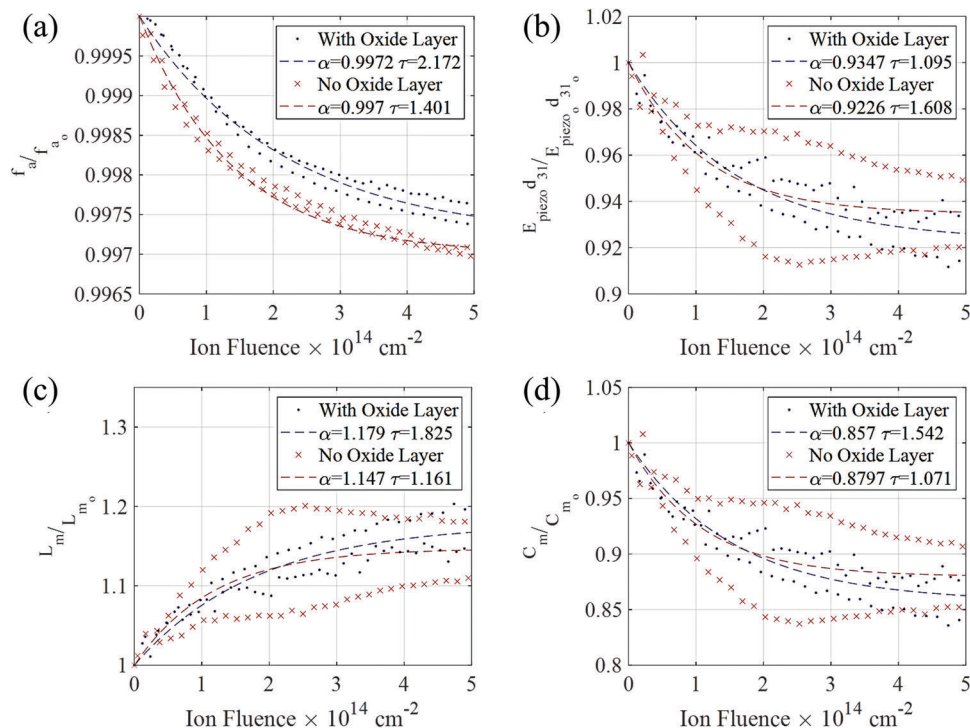


**Figure 9.** a) Fractional shift in the measured anti-resonance frequency. b) Extracted fractional shift to the product  $E_{\text{piezo}31}d_{31o}$ . c,d) Extracted fractional shift to  $L_m$  and  $C_m$ , respectively. For clarity, only one out of every ten datapoints are plotted.

ion fluence, as shown in Figures 6 and 7 and summarized in Table 3. Consequently, the reduction in quality factor leads to an increase in the motional resistances of the resonators. This relationship is mathematically substantiated by Equation (2).

The impact of  $\text{Si}^+$  ion irradiation extended beyond altering the motional impedances of the resonators; it also affected the inherent static electrical capacitances of these resonators, as demonstrated in Figure 10. The static capacitance,  $C_s$ , is inversely proportional to the resonator's electromechanical coupling coefficient.<sup>[62]</sup> Consequently, a decrease in the static capacitances of the resonators leads to an increase in their electromechanical coupling coefficients.

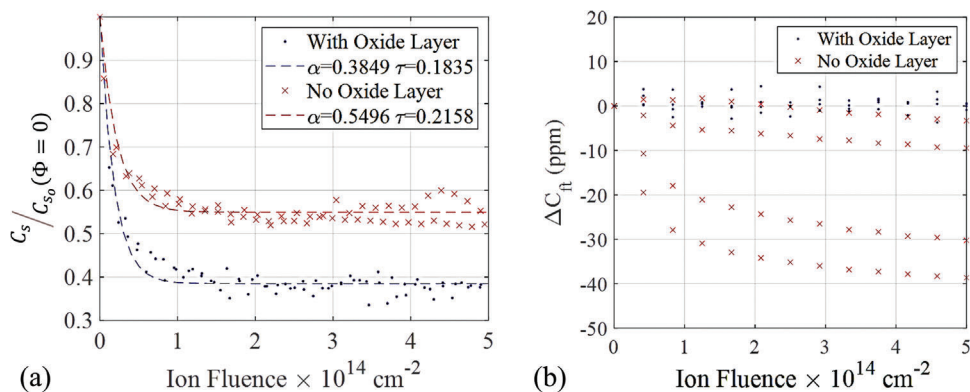


**Figure 10.** Fractional shift in (a) measured static capacitance and b) measured feedthrough capacitance. For clarity, only one out of every ten datapoints are plotted.

## 6. Conclusion

This work examines the impact of heavy ion irradiation on piezoelectrically actuated MEMS resonators. These resonators, used in applications such as navigation accelerometers, RF filters, energy harvesters, and vibration detectors, boast a small footprint, low power consumption, and minimal weight, making them suitable for compact applications including CubeSats, drones, micro UAVs, and microrobots, which often operate in hostile conditions like varying pressure, temperature, vibration, and radiation environments. Given the diversity of MEMS materials, designs, operating principles, and applications, characterizing the effects of radiation on MEMS poses significant challenges.

Though previous studies have empirically investigated various radiation effects on MEMS, this work introduces a theoretical method to characterize the behavior of RF MEMS resonator parameters under heavy ion irradiation using specific damage coefficients akin to those employed in describing radiation effects on CMOS transistors and other semiconductor devices.

AlN-transduced resonators were irradiated by 2 MeV Si<sup>+</sup> ions up to a fluence of  $5 \times 10^{14} \text{ cm}^{-2}$  at different fluxes to demonstrate this characterization method. Different designs were irradiated and studied; in addition to the AlN-on-Si design, an AlN-SiO<sub>2</sub>-Si design was irradiated. S-parameters were measured in situ to capture the changes to device parameters during irradiation. Key performance parameters,  $f_r$ ,  $f_a$ ,  $R_m$ ,  $C_m$ ,  $L_m$ ,  $C_o$ ,  $Q$ , and  $k_{\text{eff}}^2$ , were extracted, and their behavior during the irradiation period was examined. The changes to the piezoelectric parameter,  $d_{31}$ , are also observed. Damage coefficients were fit to the decaying exponential model for all parameters. The changes to the parameters caused by the radiation are well characterized by a decaying exponential. Ion flux did not appear to affect  $f_r$ , but it did affect  $R_m$ ,  $Q$ , and  $k_{\text{eff}}^2$ . Additionally, post-irradiation device recovery effects were examined and characterized using the same methodology. Recovery is also well characterized by the decaying exponential model.

This study introduces a theory-based method for characterizing the behavior of MEMS in a radiation environment, employing two damage coefficients:  $\alpha$  and  $\tau$ . The coefficient  $\alpha$  denotes the fractional change in the parameter at full saturation, in other words, when the total dose tends toward infinity ( $\Phi \rightarrow \infty$ ). Meanwhile,  $\tau$  is a decay constant that represents the fluence at which the parameter changes by a factor of  $(1 - e^{-1})$ , or  $\approx 63\%$ . These damage coefficients can be used to describe the behavior of a variety of MEMS devices, including piezoelectric, electrostatic, thermal, and electromagnetic types. Presenting a practical method for comparing different MEMS designs and materials in a radiation environment, these coefficients may stimulate further research, such as in-depth investigation of the first-principle derivations of the damage coefficients. Additionally, a more detailed assessment of the changes in damage coefficients as a function of flux could be considered. This characterization method should also be validated across other MEMS materials and operational principles. Its potential applicability extends beyond the realm of MEMS, potentially informing studies of radiation effects in other domains, including medicine. For instance, the elastic modulus of specific organic materials exposed to X-rays might be characterized in a similar manner.<sup>[63]</sup>

## Supporting Information

Supporting Information is available from the Wiley Online Library or from the author.

## Acknowledgements

The authors would like to acknowledge the support of the Ion Beam Laboratory at Sandia National Labs and the assistance of Danielle Martinez, Bas Vaandrager, Dr. Jossue Montes, and Dr. Edward Bielejec. The authors would also like to thank the Air Force Research Labs (AFRL) Sensors Directorate for their support and, particularly, Dr. Matthew Hagedon for assisting with the laser dicing of the resonators and Thomas Taylor for assisting

with the wire bonding. Finally, the authors thank the AFRL Materials and Manufacturing Directorate and the assistance of Dr. Derek Bas and Dr. Piyush Shah for their help with the PCB design. The views expressed in this paper are those of the authors and do not reflect the official policy or position of the United States Air Force, Department of Defense, or the US Government. This work was performed, in part, at the Center for Integrated Nanotechnologies, an Office of Science User Facility operated for the U.S. Department of Energy (DOE) Office of Science. Sandia National Laboratories is a multimission laboratory managed and operated by the National Technology & Engineering Solutions of Sandia, LLC, a wholly owned subsidiary of Honeywell International, Inc., for the U.S. DOE's National Nuclear Security Administration under contract DE-NA-0003525. The views expressed in the article do not necessarily represent the views of the U.S. DOE or the United States Government.

## Conflict of Interest

The authors declare no conflict of interest.

## Data Availability Statement

The data that support the findings of this study are available from the corresponding author upon reasonable request.

## Keywords

heavy particle radiation, microelectromechanical resonators, piezoelectric resonators, radiation effects in electronics, radiation effects in microelectromechanical systems

Received: March 21, 2023

Revised: July 20, 2023

Published online: August 30, 2023

- [1] G. Chen, M. Rinaldi, *J. Microelectromech. Syst.* **2020**, 29, 148.
- [2] R. Lu, S. Gong, *J. Micromech. Microeng.* **2021**, 31, 114001.
- [3] H. Chandralim, S. A. Bhave, R. Polcawich, J. Pulskamp, D. Judy, R. Kaul, M. Dubey, *Appl. Phys. Lett.* **2008**, 93, 233504.
- [4] S. Rassay, D. Mo, C. Li, N. Choudhary, C. Forgey, R. Tabrizian, *IEEE Electron Device Lett.* **2021**, 42, 1065.
- [5] H. Chandralim, D. Weinstein, L. F. Cheow, S. A. Bhave, *Sens. Actuators, A* **2007**, 136, 527.
- [6] A. Ansari, M. Rais-Zadeh, *IEEE Electron Device Lett.* **2014**, 35, 1127.
- [7] G. Piazza, P. J. Stephanou, A. P. Pisano, *J. Microelectromech. Syst.* **2007**, 16, 319.
- [8] H. Chandralim, S. A. Bhave, R. G. Polcawich, J. S. Pulskamp, R. Kaul, *IEEE Trans. Ultrason. Ferroelectr. Freq. Control* **2010**, 57, 2035.
- [9] M. Hodjat-Shamami, F. Ayazi, *Microsyst. Nanoeng.* **2020**, 6, 108.
- [10] K. Obitani, K. Araya, M. Yachi, T. Tsuchiya, *J. Microelectromech. Syst.* **2021**, 30, 384.
- [11] H. Mansoorzare, A. Todi, S. Moradian, R. Abdolvand, in *2020 IEEE International Ultrasonics Symposium (IUS)*, IEEE, Piscataway, NJ **2020**, pp. 1–4.
- [12] S. Das, A. Kumar, A. Kumar, J. Singh, R. Jha, M. Kumar, *IEEE Trans. Electron Devices* **2021**, 68, 2791.
- [13] X. Bian, H. Jin, X. Wang, S. Dong, G. Chen, J. K. Luo, M. J. Deen, B. Qi, *Sci. Rep.* **2015**, 5, 9123.
- [14] G. Lee, D. Lee, J. Park, Y. Jang, M. Kim, J. Rho, *Commun. Phys.* **2022**, 5, 94.
- [15] H.-C. Song, S.-W. Kim, H. S. Kim, D.-G. Lee, C.-Y. Kang, S. Nahm, *Adv. Mater.* **2020**, 32, 2002208.

- [16] T. Zhang, H. Liang, Z. Wang, C. Qiu, Y. B. Peng, X. Zhu, J. Li, X. Ge, J. Xu, X. Huang, J. Tong, J. Ou-Yang, X. Yang, F. Li, B. Zhu, *Sci. Adv.* **2022**, *8*, eabk0159.
- [17] H. Chandralalim, S. A. Bhave, R. G. Polcawich, J. Pulskamp, R. Kaul, *IEEE Electron Device Lett.* **2009**, *30*, 1296.
- [18] A. Gao, K. Liu, J. Liang, T. Wu, *Microsyst. Nanoeng.* **2020**, *6*, 74.
- [19] L. Hackett, M. Miller, F. Brimigion, D. Dominguez, G. Peake, A. Tauke-Pedretti, S. Arterburn, T. A. Friedmann, M. Eichenfield, *Nat. Commun.* **2021**, *12*, 2769.
- [20] D. Y. Park, D. J. Joe, D. H. Kim, H. Park, J. H. Han, C. K. Jeong, H. Park, J. G. Park, B. Joung, K. J. Lee, *Adv. Mater.* **2017**, *29*, 1702308.
- [21] Z. Yi, Z. Liu, W. Li, T. Ruan, X. Chen, J. Liu, B. Yang, W. Zhang, *Adv. Mater.* **2022**, *34*, 2110291.
- [22] G. L. Smith, J. S. Pulskamp, L. M. Sanchez, D. M. Potrepka, R. M. Proie, T. G. Ivanov, R. Q. Rudy, W. D. Nothwang, S. S. Bedair, C. D. Meyer, R. G. Polcawich, *J. Am. Ceram. Soc.* **2012**, *95*, 1777.
- [23] Q. Zhao, S. Liu, J. Chen, G. He, J. Di, L. Zhao, T. Su, M. Zhang, Z. Hou, *Rob. Auton. Syst.* **2021**, *140*, 103733.
- [24] H. Kim, S. Kerrigan, M. Bourham, X. Jiang, *IEEE Trans. Ind. Electron.* **2021**, *68*, 5346.
- [25] Y. Wang, L. Qiu, Y. Luo, R. Ding, F. Jiang, *Mech. Syst. Signal Process.* **2020**, *141*, 106730.
- [26] T. L. Naing, T. O. Rocheleau, E. Alon, C. T.-C. Nguyen, *IEEE Trans. Ultrason. Ferroelectr. Freq. Control* **2020**, *67*, 1377.
- [27] H. R. Shea, *J. Micro/Nanolithogr., MEMS, MOEMS* **2009**, *8*, 031303.
- [28] R. M. R. Pinto, V. Gund, R. A. Dias, K. K. Nagaraja, K. B. Vinayakumar, *J. Microelectromech. Syst.* **2022**, *31*, 500.
- [29] J. Wang, M. Park, S. Mertin, T. Pensala, F. Ayazi, A. Ansari, *J. Microelectromech. Syst.* **2020**, *29*, 741.
- [30] S. Shahraimi, H. Mansoorzare, A. Mahigir, R. Abdolvand, *J. Microelectromech. Syst.* **2020**, *29*, 296.
- [31] C. Fei, X. Liu, B. Zhu, D. Li, X. Yang, Y. Yang, Q. Zhou, *Nano Energy* **2018**, *51*, 146.
- [32] G. Piazza, V. Felmetzger, P. Muralt, R. H. O. Iii, R. Ruby, *MRS Bull.* **2012**, *37*, 1051.
- [33] S. Dey, S. Jejurikar, S. K. Bhattacharya, A. Banerji, K. P. Adhi, C. V. Dharmadhikari, *J. Appl. Phys.* **2010**, *108*, 094510.
- [34] H. R. Shea, in *Reliability, Packaging, Testing, and Characterization of MEMS/MOEMS and Nanodevices X*, SPIE, Bellingham, WA **2011**, pp. 96–108.
- [35] A. Holmes-Siedle, L. Adams, *Handbook of Radiation Effects*, Oxford University Press, Oxford, England **2002**.
- [36] P. Gkotsis, V. Kilchytska, U. Bhaskar, O. Militaru, X. Tang, C. Fragkiadakis, P. B. Kirby, J.-P. Raskin, D. Flandre, L. A. Francis, *Procedia Eng.* **2011**, *25*, 172.
- [37] K. Holbert, S. S. McCready, A. Sharif Heger, T. H. Harlow, D. R. Spearing, in *American Nuclear Society 4th International Topical Meeting on Nuclear Plant Instrumentation, Control and Human Machine Interface Technology*, **2004**, pp. 43.
- [38] M. A. Hopcroft, W. D. Nix, T. W. Kenny, *J. Microelectromech. Syst.* **2010**, *19*, 229.
- [39] L. B. Freund, S. Suresh, *Thin Film Materials: Stress, Defect Formation and Surface Evolution*, Cambridge University Press, Cambridge, England **2004**.
- [40] J. S. Custer, M. O. Thompson, D. C. Jacobson, J. M. Poate, S. Roorda, W. C. Sinke, F. Spaepen, *Appl. Phys. Lett.* **1994**, *64*, 437.
- [41] A. R. Knudson, S. Buchner, P. McDonald, W. J. Stapor, A. B. Campbell, K. S. Grabowski, D. L. Knies, S. Lewis, Y. Zhao, *IEEE Trans. Nucl. Sci.* **1996**, *43*, 3122.
- [42] A. Crunteanu, A. Pothier, P. Blondy, F. Dumas-Bouchiat, C. Champeaux, A. Catherinot, P. Tristant, O. Vendier, C. Drevon, J. L. Cazaux, L. Marchand, *Microelectron. Reliab.* **2006**, *46*, 1741.
- [43] D. D. Lynes, H. Chandralalim, J. E. Bevins, J. C. Petrosky, *Adv. Eng. Mater.* **2023**, *25*, 2201837.
- [44] L. Wang, Q. A. Huang, J. Tang, J. Luo, in *2009 16th IEEE International Symposium on the Physical and Failure Analysis of Integrated Circuits*, IEEE, Piscataway, NJ **2009**, pp. 764–767.
- [45] S. T. Patton, A. J. Frasca, J. W. Talnagi, D. J. Hyman, B. S. Phillips, J. G. Jones, R. A. Vaia, A. A. Voevodin, *IEEE Trans. Nucl. Sci.* **2013**, *60*, 3074.
- [46] V. Belwanshi, S. Philip, A. Topkar, *IEEE Trans. Nucl. Sci.* **2019**, *66*, 2055.
- [47] J.-T. Lin, P. Wang, P. Shuvra, S. McNamara, M. McCurdy, J. Davidson, K. Walsh, M. Alles, B. Alphenaar, in *33rd International Conference on Micro Electro Mechanical Systems (MEMS)*, IEEE, Piscataway, NJ **2020**, pp. 968–971.
- [48] J. Lee, M. J. Krupcale, P. X.-L. Feng, *Appl. Phys. Lett.* **2016**, *108*, 023106.
- [49] W. Sui, X.-Q. Zheng, J.-T. Lin, J. Lee, J. L. Davidson, R. A. Reed, R. D. Schrimpf, B. W. Alphenaar, M. L. Alles, P. X.-L. Feng, *IEEE Trans. Nucl. Sci.* **2022**, *69*, 216.
- [50] J. Gomes, H. R. Shea, in *Reliability, Packaging, Testing, and Characterization of MEMS/MOEMS and Nanodevices X*, SPIE, Bellingham, WA **2011**, pp. 126.
- [51] H. Chen, H. Jia, W. Liao, V. Pashaei, C. N. Arutt, M. W. McCurdy, C. A. Zorman, R. A. Reed, R. D. Schrimpf, M. L. Alles, P. X.-L. Feng, *Appl. Phys. Lett.* **2019**, *114*, 101901.
- [52] H. Y. Tada, J. R. Carter, B. E. Anspaugh, R. G. Downing, *Solar Cell Radiation Handbook* **1982**, <https://ntrs.nasa.gov/citations/19830006416>.
- [53] *Piezoelectric MEMS Resonators*, (Eds: H. Bhugra, G. Piazza, Springer, Berlin **2017**).
- [54] H. Chandralalim, S. A. Bhave, R. G. Polcawich, J. S. Pulskamp, R. Kaul, in *International Ultrasonics Symposium*, IEEE, Piscataway, NJ **2009**, pp. 2145–2148.
- [55] G. H. Kinchin, R. S. Pease, *Rep. Prog. Phys.* **1955**, *18*, 301.
- [56] G. Pillai, S.-S. Li, *IEEE Sens. J.* **2021**, *21*, 12589.
- [57] S. R. Logan, *J. Chem. Educ.* **1982**, *59*, 279.
- [58] H. Wilski, *Int. J. Radiat. Appl. Instrum. Part C. Radiation Phys. Chem.* **1987**, *29*, 1.
- [59] A. N. Hamoud, J. R. Laghari, B. Krishnakumar, *IEEE Trans. Nucl. Sci.* **1987**, *34*, 1822.
- [60] D. D. Lynes, H. Chandralalim, *Adv. Mater. Interfaces* **2023**, *10*, 2202446.
- [61] D. A. Parks, B. R. Tittmann, *IEEE Trans. Ultrason. Ferroelectr. Freq. Control* **2014**, *61*, 1216.
- [62] M. Rinaldi, C. Zuniga, C. Zuo, G. Piazza, *IEEE Trans. Ultrason. Ferroelectr. Freq. Control* **2010**, *57*, 38.
- [63] E. Spyratou, M. Dilvoi, G. Patatoukas, K. Platoni, M. Makropoulou, E. P. Efstathopoulos, *J. Med. Phys.* **2019**, *44*, 113.

# ADVANCED MATERIALS INTERFACES

---

Open Access

## Supporting Information

for *Adv. Mater. Interfaces*, DOI 10.1002/admi.202300240

Impact of Silicon Ion Irradiation on Aluminum Nitride-Transduced Microelectromechanical Resonators

*David D. Lynes\**, *Joshua Young*, *Eric Lang* and *Hengky Chandralim\**

# Supporting Information

## Impact of silicon ion irradiation on aluminum nitride-transduced microelectromechanical resonators

David D. Lynes<sup>1,\*</sup>, Joshua Young<sup>2</sup>, Eric Lang<sup>3</sup>, and Hengky Chandralim<sup>1,\*</sup>

<sup>1</sup>Department of Electrical and Computer Engineering  
Air Force Institute of Technology,  
Wright-Patterson Air Force Base, OH 45433, USA

<sup>2</sup>Ion Beam Laboratory  
Sandia National Laboratories  
Albuquerque, NM 87123, USA

<sup>3</sup>Department of Nuclear Engineering  
The University of New Mexico  
Albuquerque, NM 87131, USA

\*Corresponding Authors:  
david.lynes.2@us.af.mil  
hengky@microsystems.group

## S.1 Sample Preparation

An image of the prepared sample, a resonator mounted to a custom PCB, is presented in Figure S1.



Figure S1. Example of a diced chip mounted on PCB and prepared for irradiation.

## S.2 Atomic displacement energies

The specific displacement energies for the constituent elements used in the TRIM simulations of the resonators irradiated by 2 MeV Si<sup>+</sup> ions are presented in Table S1.

Table S1. Displacement Energies of Constituent Elements Used in TRIM Simulations

Al	Cr	N	Si	O
25 eV	25 eV	28 eV	15 eV	28 eV

## S.3 Measured Data

The measured values of  $f_r$ ,  $R_m$ ,  $Q$ , and  $k_{eff}^2$  for the resonators after irradiation to a fluence of  $5 \times 10^{14} \text{ cm}^{-2}$  at a flux of  $1.9 \times 10^{11} \text{ cm}^{-2} \text{ s}^{-1}$  are presented in Figure S2. The expected decaying exponential characteristic of  $R_m$ ,  $Q$ , and one port  $k_{eff}^2$  as a function of ion fluence can be seen in the data.

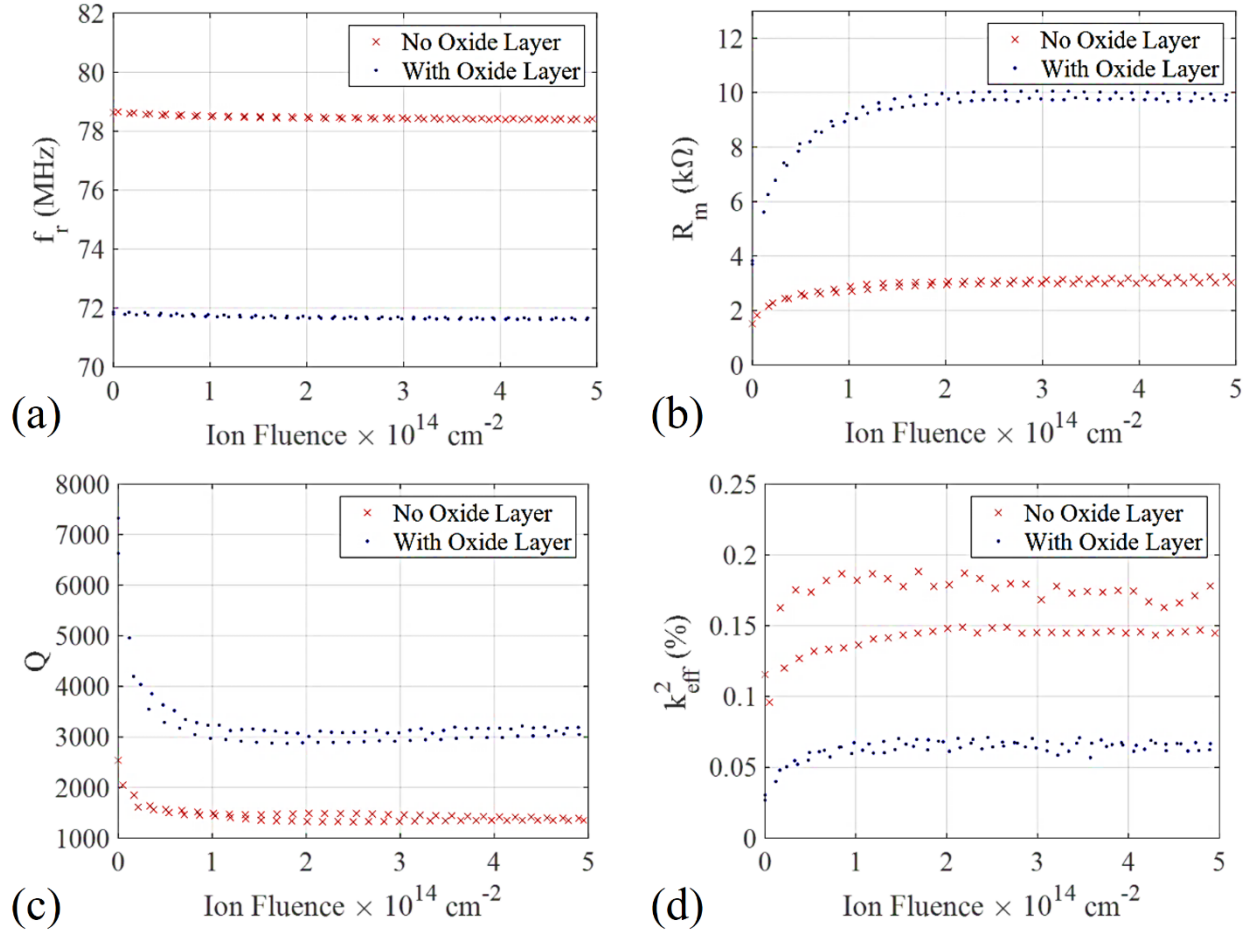


Figure S2. Measured values of (a)  $f_r$ , (b)  $R_m$ , (c)  $Q$ , (d) and  $k_{eff}^2$  for the resonators irradiated with 2 MeV  $\text{Si}^+$  ions at a flux of  $1.9 \times 10^{11} \text{ cm}^{-2} \text{ s}^{-1}$  to a total fluence of  $5 \times 10^{14} \text{ cm}^{-2}$ . The decaying exponential characteristics of  $R_m$ ,  $Q$ , and  $k_{eff}^2$  are readily apparent. For clarity, only one out of every 10 datapoints are plotted.

#### S.4 Pre- and Post- Irradiation Material Analysis

Prior to Raman and EBSD analysis, the samples are cleaned using a 30 second acetone rinse, 30 second methanol rinse, 30 second isopropanol rinse, and blow-dried with nitrogen. The surface silicon exposed to the 2 MeV  $\text{Si}^+$  ions is then analyzed by Raman spectroscopy and electron backscatter diffraction (EBSD). An image of the ion beam superimposed over the target device is shown in Figure S3 (a). The dark areas, as indicated by the arrows in the figure, are n-Si exposed to the ion beam. The Raman spectroscopy is done using a 532 nm laser. The average pre- (blue)

and post- (red) irradiation spectra are shown in Figure S3 (b). The non-irradiated n-Si exhibited a significant peak at  $521\text{ cm}^{-1}$  which is typical of highly crystalline Si. As crystalline Si is amorphized, the  $521\text{ cm}^{-1}$  peak shrinks and a broad band forms centered at  $480\text{ cm}^{-1}$ .<sup>[1]</sup> The post-irradiated n-Si exhibited a peak of significantly smaller intensity at  $521\text{ cm}^{-1}$ , but no broad peak at  $480\text{ cm}^{-1}$ . Therefore, there is evidence to support the occurrence of some dislocation damage, but far from enough to consider the material near-amorphous.

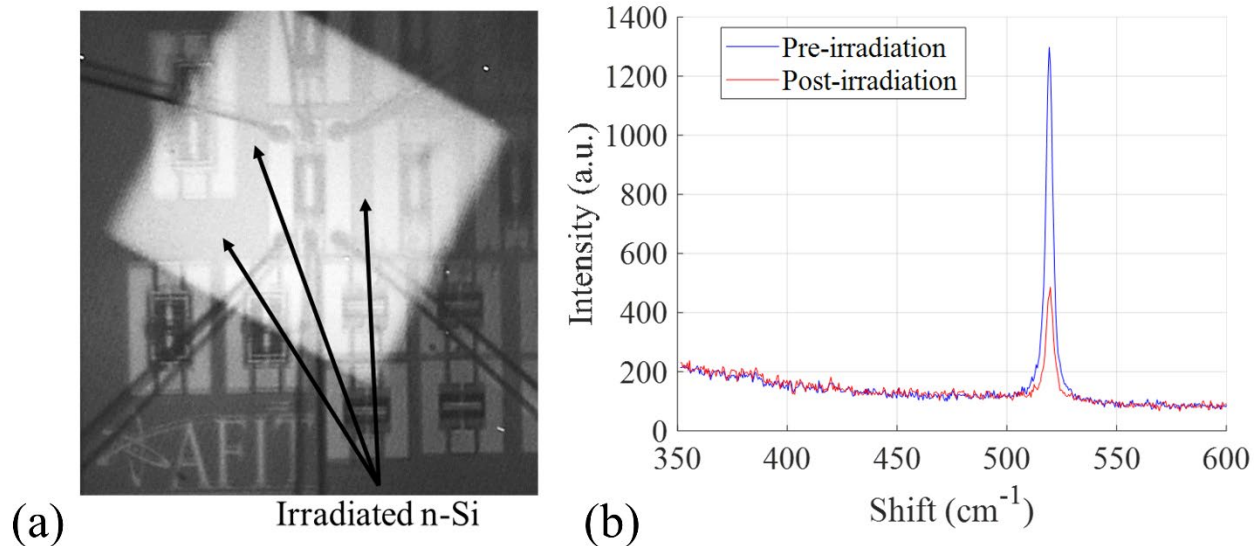


Figure S3. (a) Irradiated areas of surface n-Si where Raman and EBSD analysis was performed. (b) Average Raman spectra of surface n-Si pre- and post-irradiation.

EBSD analysis also provides insight into the defected near-surface of the irradiated silicon. The samples were prepared in the same manner as they were for the Raman spectroscopy and EBSD analysis was performed on the exposed surface n-Si away from the resonators, as indicated by the black arrows in Figure S3 (a). EBSD is collected using an Oxford Instruments Symmetry S3 detector coupled with AZtecHKL data acquisition software. Electron beam acceleration voltage is 20 kV, probe current is 2.2 nA, working distance is 13.3 mm, and acquisition rate is approximately 920 Hz. EBSD analysis is performed using AZtecCrystal. Disorientation/texture

analysis shows the degree of alignment of crystal lattices detected in the sample. The incremental change plot, presented in Figure S4, presents the average of 6 line scans of the surface of the samples. The plot shows some evidence of crystallographic changes to the surface silicon post-irradiation. Incremental pole figures (IPF-Z) obtained from EBSD also provide awareness into the level of disorientation in the surface silicon. Figure S5 shows the IPFs for (a) unirradiated and (b) irradiated samples. While some carbon contamination is still present on the post-irradiation sample after cleaning, EBSD provides some insight into the effects of the  $\text{Si}^+$  ion irradiation to the surface of the n-Si substrate.

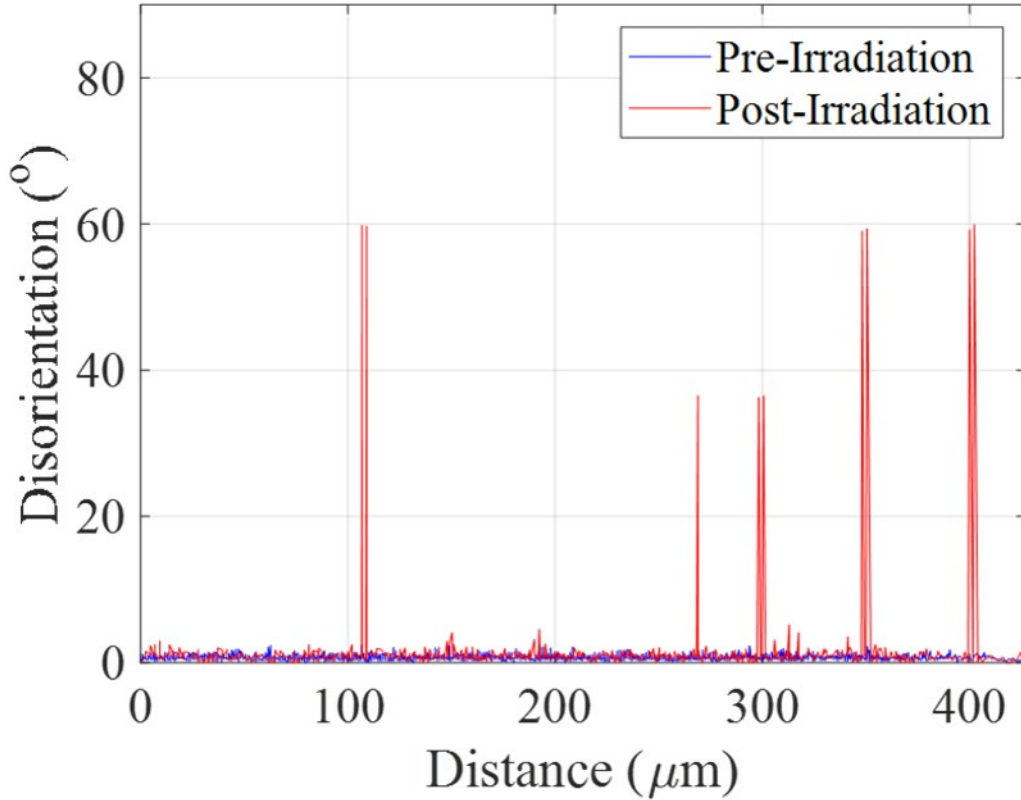


Figure S4. EBSD average disorientation analysis of surface silicon pre- and post-irradiation.

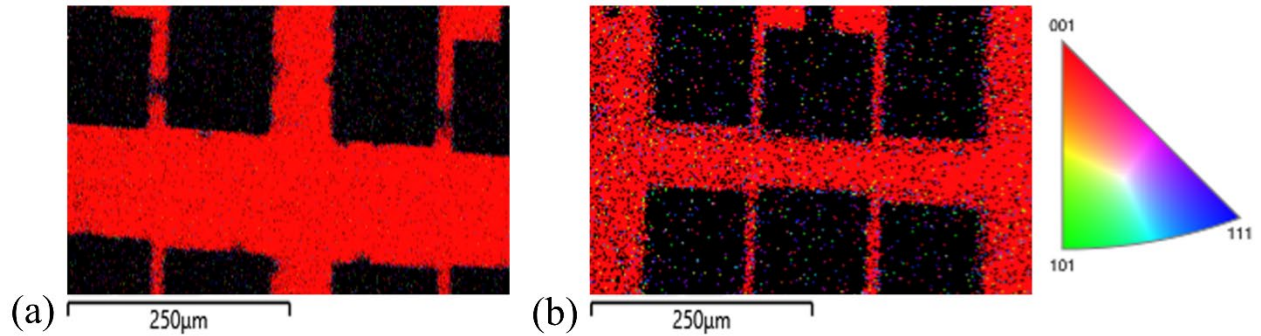


Figure S5. EBSD obtained IPF-Z map of surface silicon (a) pre- and (b) post-irradiation. Surface silicon is shown in red.

Transmission electron microscopy (TEM) analysis is performed on pre- and post-irradiated samples. TEM samples are made via focused ion beam (FIB) liftout process with a Scios 2 DualBeam FIB using a Ga ion beam operated at 30 kV with final thinning at 5 kV. An SEM micrograph of the TEM liftout location is presented in Figure S6. TEM analysis is performed with a FEI Titan ETEM G2 operated at 300 kV. An example of the analysis is presented in Figure S7. The left column indicates a pristine (pre-irradiation) sample. In the right column is a post-radiation sample. The TRIM results are superimposed on the cross-sectional image. These images provide an indication of a decrease in long-range order of the crystalline Si and AlN during irradiation. It should be noted, however, that a significant amount of TEM images provided little indication of change to long-range order. Therefore, the change in defect density caused by the irradiation is extremely small to be detectable via TEM in a practical sense.

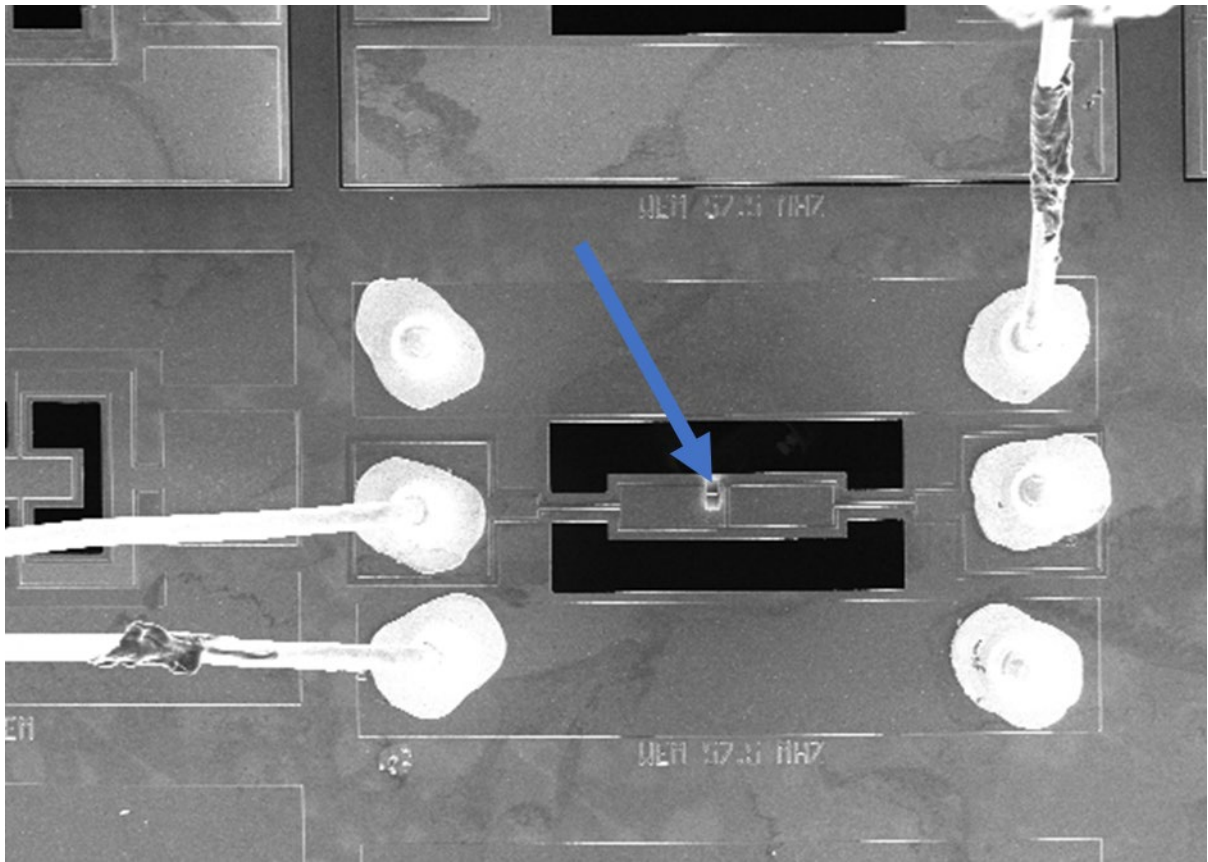


Figure S6. SEM micrograph of the FIB liftout location.

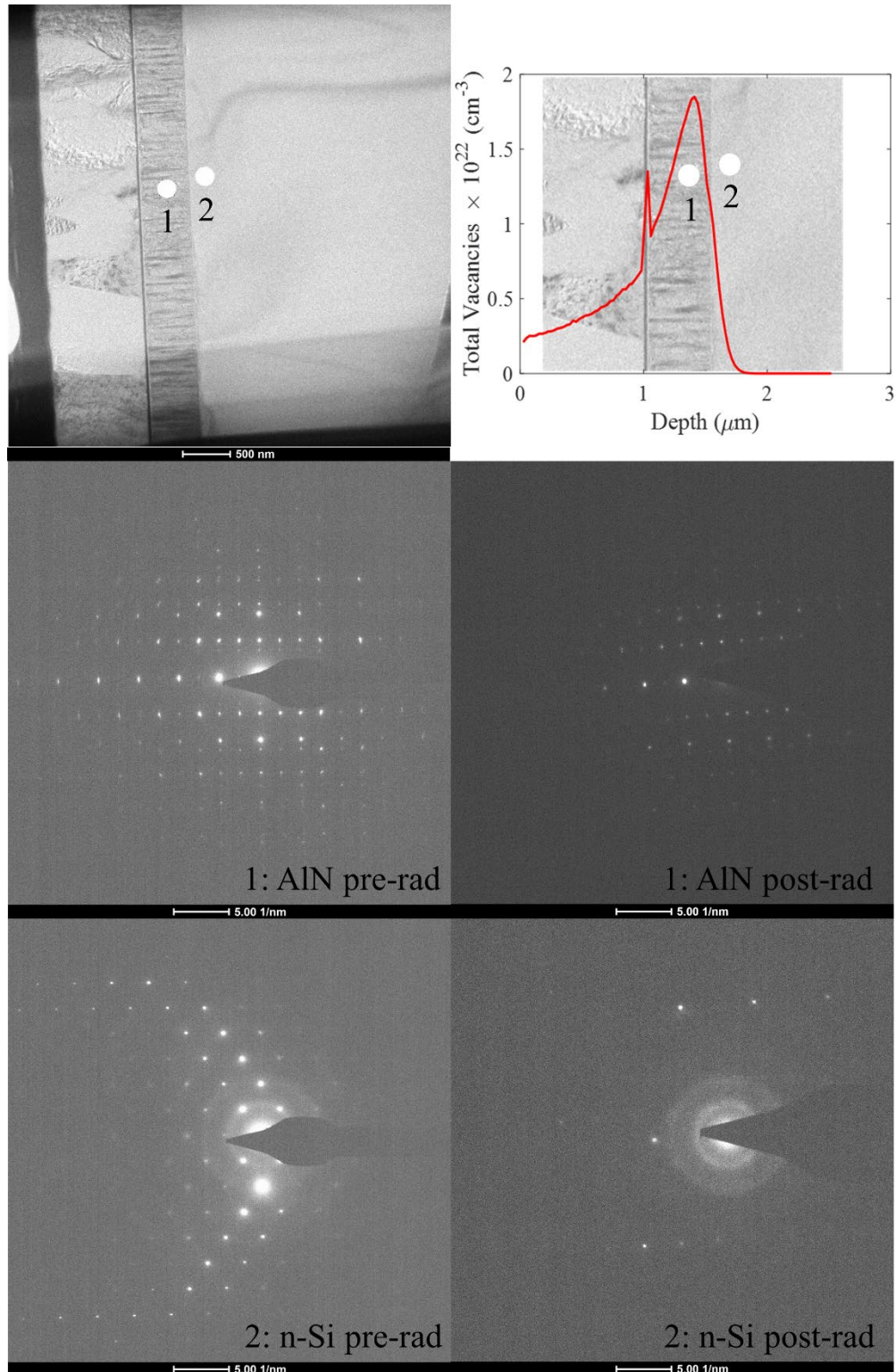


Figure S7. TEM analysis of a cross-sectional sample of a rectangular flat plate AlN-on-Si resonator pre- (left) and post- (right) 2 MeV  $\text{Si}^+$  ion irradiation. Total dose was  $5 \times 10^{14} \text{ cm}^{-2}$  at  $190 \times 10^9 \text{ cm}^{-2} \text{ s}^{-1}$ . TRIM simulation results are superimposed over the cross-sectional image.

Overall, the first order differential equation presented in (7) is suitable to describe the change in device behavior due to irradiation. With the exception of  $k_{eff}^2$  the decaying exponential fit the data exceptionally well with  $R^2$  values better than 0.9. Furthermore, equation (7) also is adequate at capturing rebound behavior. Analytical analysis supports the conclusion that the change to  $f_r$  is predominantly due to changes in the atomic structure caused by  $\text{Si}^+$  ion irradiation. The implantation of  $\text{Si}^+$  ions in the dielectric layers alters the effective permittivity of the dielectric layer. Post-irradiation effects can be detected via Raman spectroscopy, EBSD, and TEM.

## References

- [1] T. Deschaines, J. Hodkiewicz, P. Henson, *Thermo Sci.* **2009**, 3.